

Employing the dynamics of the electrochemical interface at aqueous zinc-ion battery cathode

Nigel Becknell

Argonne National Laboratory <https://orcid.org/0000-0001-7857-6841>

Pietro Lopes

Argonne National Laboratory <https://orcid.org/0000-0003-3211-470X>

Toru Hatsukade

Argonne National Laboratory

Xiuquan Zhou

Argonne National Laboratory

Yuzi Liu

Argonne National Laboratory <https://orcid.org/0000-0002-8733-1683>

Brandon Fisher

Argonne National Laboratory

Duck Young Chung

Argonne National Laboratory <https://orcid.org/0000-0002-1315-2631>

Mercouri Kanatzidis

Northwestern University

Nenad Markovic

Argonne National Laboratory

Sanja Tepavcevic (✉ sanja@anl.gov)

Argonne National Lab <https://orcid.org/0000-0003-0151-8832>

Vojislav Stamenkovic (✉ v.stamenkovic@uci.edu)

University of California Irvine <https://orcid.org/0000-0002-1149-3563>

Article

Keywords: energy storage device, electrochemical interface, aqueous zinc-ion batteries, durability

Posted Date: January 4th, 2021

DOI: <https://doi.org/10.21203/rs.3.rs-111489/v1>

License:   This work is licensed under a Creative Commons Attribution 4.0 International License.

[Read Full License](#)

Abstract

Intrinsically stable materials are desirable for constructing energy storage devices, which aim to demonstrate durability under the harsh electrochemical conditions that are detrimental to their lifespan. However, we demonstrate here that the intrinsic instability of an electrochemical interface can be converted from an obstacle into an advantage. In aqueous zinc-ion batteries, manganese oxide (MnO_2) exhibits considerable dissolution even in electrolyte containing Mn^{2+} salt. Balancing with redeposition alleviates the harmful impact of dissolution on performance and alters the trajectory of the active phase. Inclusion of Mn^{2+} salt in the electrolyte induces MnO_2 deposition on all conductive surfaces, requiring that distracting side reactions be eliminated to isolate the dynamics of the active phase. Under conditions favoring dissolution, capacity decreases dramatically and a highly crystalline tetragonal ZnMn_2O_4 phase forms, while redeposition helps maintain capacity and promotes a disordered cubic Zn-rich phase. Ultimately, this work aims to illuminate a path forward to unlock the potential of batteries made with materials that are fundamentally unstable in their operating environment.

Introduction

Energy storage technologies offer immense flexibility and resilience for the electrical grid¹⁻³. The current focus in research and development as well as techno-economic evaluations is mainly on lithium-ion, sodium-sulfur, lead-acid, redox-flow, and nickel-based battery chemistries²⁻⁴. Each of these chemistries comes with fundamental drawbacks that limit mass deployment of these technologies in the future electric grid. The extensive list of obstacles includes reliance on scarce elements, toxic materials, flammable electrolytes, temperature restrictions, durability issues, and/or low energy densities²⁻⁶. For those reasons, consideration of additional chemistries is desired and has recently drawn attention to the aqueous Zn-ion battery (AZIB), which is low-cost, safe, and environmentally friendly⁷⁻¹¹. The Zn metal anode in the AZIB brings 820 mAh/g theoretical capacity¹⁰ and resistance to hydrogen evolution in aqueous electrolytes¹¹. Research on AZIB cathodes consists of studies on materials such as vanadium-based oxides^{12,13}, zinc or copper hexacyanoferrates^{14,15}, and manganese oxides^{5,11,16-18}. Manganese oxides are abundant, cost effective, safe, non-toxic, and versatile due to the accessibility of multivalent states and the many possible polymorphs of manganese (IV) oxide (MnO_2)^{5,11,19}. The theoretical capacity of a MnO_2 cathode can range from 308 mAh/g to 616 mAh/g for a one- to two-electron reduction of Mn^{4+} . Nevertheless, retaining the cathode performance over a long period remains a challenge for future utilization of Zn/ MnO_2 AZIB technology for commercial applications.

The predominant approach to engineering a battery material has been to control its structure such that the framework will not change throughout the lifetime of the battery. Therefore, battery electrode materials are typically designed to be as stable as possible to minimize dissolution, which can cause loss of the intercalation host or the delicate control of its phase and composition. Dissolution of transition metals such as Mn, Co, Ni, Fe, and V from the cathode has been widely observed in various metal-ion

batteries and induces secondary capacity fading processes at Li-ion battery anodes^{20,21}. Dissolution has made such a deleterious impact on long-term battery performance that significant effort has been devoted to preventing it through precise compositions, protective coatings, surface doping, or electrolyte engineering²²⁻²⁵. In Zn/MnO₂ AZIBs, MnO₂ dissolution was suspected to play a key role in capacity fading due to the loss of cathode active material^{8,9,26,27}. The main strategy employed to address this issue was to include Mn²⁺ in the electrolyte, which was proposed to deter further dissolution and preserve the initial functionality of the cathode material²⁸⁻³⁰. Indeed, the inclusion of a Mn²⁺ salt improves capacity retention over long-term cycling of AZIBs^{26,28-30}. However, the presumed mechanism that the additive simply inhibits dissolution is unlikely because the equilibrium between solid MnO₂ and Mn²⁺_(aq) is constantly shifting during cycling. Therefore, there remains extensive insight to be gained on the impact of Mn²⁺ salt on the MnO₂ dissolution/redeposition equilibrium and on the kinetic pathways of phase changes and long-term performance.

This report illustrates how dissolution, once seen as a fundamental drawback for MnO₂ cathodes, can fortify capacity in AZIBs. Moreover, the dissolution and redeposition of MnO₂ is shown to be a key kinetic pathway for the phase changes observed in the cathode active material. The intricacies and functionality of the dynamic MnO₂ cathode were uncovered only after isolating its behavior from side reactions that occur when introducing active material into the liquid phase of an AZIB. Finally, this work provides guidance for implementing specific mechanisms in an AZIB that will enable wide deployments of this technology.

Results

Establishing the AZIB testing environment.

Figure 1a demonstrates two methods of operation for an AZIB MnO₂ cathode. In the first instance, MnO₂ (δ -MnO₂ is depicted) could be used solely as an intercalation host for Zn²⁺ cations. The cathode active material exists only in the solid phase, and the instability from MnO₂ dissolution is an obstacle to achieving the desired performance. In the second instance, the instability of MnO₂ is embraced by incorporating Mn²⁺ in the electrolyte to facilitate cycles of MnO₂ dissolution and redeposition, in addition to Zn²⁺ intercalation. The cathode material used in this study was nanostructured δ -MnO₂ (see experimental details in Methods and characterization in Supplementary Fig. 1–2, Supplementary Table 1). The δ -MnO₂ particles were encased within layers of carbon nanotubes (δ -MnO₂/CNT), which provide a high surface area, conductive, and robust support for the active material (Supplementary Fig. 3). Either 0.5 M ZnSO₄ (Zn²⁺_(aq)-only) or 0.5 M ZnSO₄/0.5 M MnSO₄ (Zn²⁺_(aq)-Mn²⁺_(aq)) electrolytes were used to explore the two mechanisms of operation. In Zn²⁺_(aq)-only electrolyte, the capacity of the δ -MnO₂/CNT cathode decreased by 54% over 100 cycles, while in Zn²⁺_(aq)-Mn²⁺_(aq) electrolyte, the capacity

increased from ~ 185 mAh/g to nearly 500 mAh/g (Fig. 1b,c). Such high capacity has only been observed a few times in Zn/MnO₂ AZIBs³¹⁻³⁴, so the mechanism behind this spike warranted further investigation.

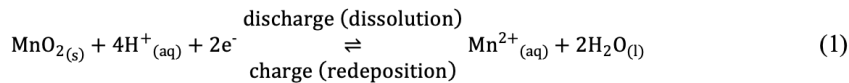
Upon disassembling a battery with Zn²⁺_(aq)-Mn²⁺_(aq) electrolyte, a thick black film was observed on the stainless steel (SS) current collector. This was an immediate indication about the consequences of using electrochemically active material in the liquid phase of an AZIB. Considering that the research on AZIBs has often adopted coin cell fabrication techniques from Li-ion battery research, including the use of SS components^{26,27,33-38}, the testing methodology needs thorough evaluation to prevent interference with the true phenomena during cycling. Therefore, potential side reactions with the supporting current collector were studied to eliminate their influence on cathode performance. This approach guarantees that the impact of MnO₂ dissolution and redeposition on phase changes, capacity, and stability of the active material can be delineated and studied.

Batteries were assembled without a MnO₂ cathode to isolate the interface between either a SS or Ti current collector and the Zn²⁺_(aq)Mn²⁺_(aq) electrolyte. Using 50 μL of electrolyte, the capacity of a battery with a SS electrode dramatically increased over the course of 100 cycles (Fig. 2a). In contrast, the capacity on a Ti cathode dropped steeply over the first 30 cycles to a negligible value. If only 10 μL electrolyte was used, the initial capacity was negligible on both Ti and SS. However, the capacity still increased over time on SS while it decreased on Ti. The increase in capacity on SS is attributed to the catalytic effect of nickel, a component in SS, on the electrodeposition of manganese oxide^{32,39-41}. The capacity from SS cells was less reproducible than Ti due to the variability of these catalytic conditions. Since it is impossible to control the electrolyte distribution within a coin cell after assembling, it is clear that Ti is the more stable and reproducible choice for AZIB studies due to its minimal effect on the cathode performance.

In concurrence with the results shown in Fig. 2a, the impact of the current collector material on the observed AZIB performance is highly dependent on the volume of electrolyte used. Recent studies have included a SS current collector at the positive electrode without reporting the precise amount of electrolyte used^{26,27,33-36}. However, it is critical to control the volume of electrolyte because adding a Mn²⁺ salt makes the liquid phase an active material that contributes capacity. The contrast between current collectors is drastic when 50 μL electrolyte is used (Fig. 2b). The δ-MnO₂/CNT cathode with SS exhibits a steep rise in capacity over 100 cycles, while the capacity increases much less dramatically with a Ti current collector. In addition to MnO₂ deposition on the metallic current collector, X-ray diffraction (XRD) confirmed that ε-MnO₂ electrodeposits on bare CNTs in this voltage region (Fig. 2c). To reduce the impact of the current collector, only 10 μL electrolyte was used, although cathodes with SS still had more improvement in capacity than Ti current collectors. It is clear that Ti should be used to support the active material in AZIB research and the volume of electrolyte should be selected after consideration of the electrode area, active mass, and geometry of the battery (see Methods for additional detail). By eliminating the increased capacity from side reactions with SS, the mechanisms for capacity evolution in AZIBs can be fairly evaluated.

Stage I of transformation of δ -MnO₂ cathode.

Since MnO₂ dissolution is prevalent under the electrochemical conditions of interest in AZIBs, the potential for MnO₂ redeposition must be leveraged to attain stable battery performance. It is important to note that in Zn²⁺_(aq)Mn²⁺_(aq) electrolyte, dissolution and redeposition can occur each cycle according to the following reaction:



The Coulombic efficiency (CE) provides information on whether the equilibrium lies further to the left or right of equation (1) in a given cycle. Initially, the δ -MnO₂/CNT cathode is charged to the upper potential limit (1.9 V vs Zn/Zn²⁺), which does not appreciably change the crystal structure (Supplementary Fig. 4). The first cycle begins with discharge, initiating Stage I of the transformation of δ -MnO₂. Therefore, CE is calculated here as the ratio of the discharge capacity to the following charge capacity (see Supplementary Note 1 and Supplementary Fig. 5 for additional detail). Within the first five cycles, the capacity peaks and the CE rises above 100% (Fig. 3a,b), indicating considerable dissolution of δ -MnO₂ in the slightly acidic Zn²⁺_(aq)-Mn²⁺_(aq) electrolyte (pH \approx 5.5). Enhanced dissolution is supported by cyclic voltammetry (CV, Fig. 3c). In Zn²⁺_(aq)-only electrolyte, the Zn²⁺-intercalation peak occurs at \sim 1.37 V and MnO₂ dissolution occurs below 1.2 V. The narrower reduction wave in the CV is attributed to Zn²⁺ intercalation due to the transport-related issues of solid-state Zn²⁺ diffusion, while the broader wave is attributed to MnO₂ dissolution due to the availability of excess solid MnO₂ at the electrochemical interface. In Zn²⁺_(aq)-Mn²⁺_(aq) electrolyte, MnO₂ dissolution is also indicated by substantial reduction current below 1.2 V in the first five cycles. From cycle 5 to 10, the magnitude of dissolution current decreases and the CV begins to stabilize, indicating that dissolution is most notable in the first 5 cycles (Supplementary Fig. 6).

Given the extensive MnO₂ dissolution taking place, it is important to establish its relationship to possible changes in the crystal structure. XRD shows that δ -MnO₂ begins converting to tetragonal spinel Zn_xMn₂O₄ after just the first discharge (Fig. 3d). XRD also exposes the presence of Zn₄(OH)₆SO₄·4H₂O (zinc hydroxide sulfate, ZHS) after discharge at cycles 1 and 5. This is further proof of the substantial MnO₂ dissolution occurring in the first five cycles. According to equation (1), MnO₂ dissolution consumes protons, raising the pH of the electrolyte^{42,43}. Various hydrates of ZHS have been observed to precipitate out of ZnSO₄ solutions at a pH above \sim 5.5⁴³⁻⁴⁵. Therefore, the presence of ZHS indicates more alkaline pH caused by MnO₂ dissolution in the first five cycles. Because the precipitation of ZHS acts as a buffer, it is estimated the pH increases to a maximum of \sim 6.0 based on *ex situ* precipitation experiments (Supplementary Fig. 7). In addition, transmission electron microscopy (TEM) shows that the architecture of interconnected sheets has completely transformed by cycle 5 due to dissolution (Fig. 3e,f). Between cycles 5 to 10, the formation of the spinel Zn_xMn₂O₄ phase likely reduces dissolution, shifting the

equilibrium of equation (1) towards deposition. The increase in ϵ -MnO₂ deposition acidifies the electrolyte, dissolving ZHS. By cycle 10, ZHS is no longer present in XRD, δ -MnO₂ barely remains, and the Zn_xMn₂O₄ crystal domains are growing.

Stage II of transformation of δ -MnO₂ cathode.

The local minimum in capacity at cycle 10 concludes Stage I, in which the instability of the active material was exemplified. Stage II provides further insight into the potential for leveraging the dynamic cathode during battery operation. The impact of the Zn²⁺_(aq)-Mn²⁺_(aq) electrolyte in Stage II is clear from CV, which is essentially steady by 30 cycles, while the current is constantly decreasing even after 30 cycles in Zn²⁺_(aq)-only electrolyte (Supplementary Fig. 8). During Stage II, the capacity initially increases and the CE approaches a limit of 99.9% by cycle 100 (Fig. 4a). The lower CE at cycle 10 indicates that ϵ -MnO₂ electrodeposition during charging is dominant. The result is a buildup of active material on the cathode that explains the steady increase in the capacity normalized to initial active mass, which peaks after approximately 55 cycles. The deviation of CE from 100% indicates that MnO₂ dissolution/redeposition is not a fully reversible process under these conditions. This is attributed to the formation of Zn_xMn₂O₄ and decreased dissolution of this phase.

As the Zn²⁺_(aq)-Mn²⁺_(aq) electrolyte is depleted of Mn²⁺, the capacity begins to fade. The XRD shows that in the discharged state at cycle 30, δ -MnO₂ has completely disappeared leaving only tetragonal spinel Zn_xMn₂O₄ (Fig. 4b). However, as the capacity fades, XRD indicates that some cubic zinc manganese oxide is forming after discharge^{46,47}. This suggests intercalation of Zn²⁺ above a 1:2 Zn:Mn ratio, which was confirmed by inductively coupled plasma-mass spectrometry (ICP-MS) of the cathode after discharge at 100 cycles (Supplementary Table 2). The charged state at 100 cycles exhibits only tetragonal ZnMn₂O₄ structure and composition, suggesting that the Zn²⁺-intercalation capacity is due to intercalation of Zn²⁺ into tetragonal spinel ZnMn₂O₄ (Supplementary Fig. 9, Supplementary Table 2). This is a low capacity process (~ 49 mAh/g theoretical based on ICP-MS), counteracting the potential for high capacity due to fresh ϵ -MnO₂ deposition and dissolution (616 mAh/g theoretical).

Comparison of the performance and phase changes of δ -MnO₂ in Zn²⁺_(aq)-only electrolyte provides additional insight into the underlying mechanisms occurring over the course of 100 cycles. Dissolution of the MnO₂ host causes the capacity to drop continuously after the first 10 cycles in Zn²⁺_(aq)-only electrolyte (Fig. 4c). Despite the dissolution, the XRD after 100 cycles indicates highly crystalline tetragonal spinel Zn_xMn₂O₄, as well as reflections associated with ZHS (Fig. 4b, Supplementary Fig. 10). The presence of ZHS proves that the equilibrium is shifted strongly towards dissolution of MnO₂ in Zn²⁺_(aq)-only electrolyte. Dissolution is also evident from analysis of the CE, which rises above 100% for the majority of the first 30 cycles, and TEM that shows complete loss of the interconnected sheets of the synthesized architecture (Supplementary Fig. 11–12). It is clear that the mechanism by which δ -MnO₂ converts to tetragonal Zn_xMn₂O₄ does not require redeposition of ϵ -MnO₂. However, high capacity is

facilitated by the constant redeposition/dissolution of ϵ -MnO₂ in Zn²⁺_(aq)Mn²⁺_(aq) electrolyte because of the difficulty in reversibly intercalating Zn²⁺ in the spinel structure^{48–50}. This provides novel understanding of the fundamental processes in a Zn/MnO₂ battery and the potential benefits of limiting Zn²⁺ intercalation.

Discussion

The complex interplay of dissolution/redeposition, electrolyte pH, and solid-state phase changes during AZIB operation is summarized in Fig. 5. During Stage I (Fig. 3), substantial dissolution of MnO₂ increases the pH and Mn²⁺ concentration in the electrolyte. The increase in pH induces precipitation of ZHS on the cathode. Simultaneously, Zn²⁺ intercalation induces a phase change to Zn_xMn₂O₄, which exhibits a lower MnO₂ dissolution rate. This allows ϵ -MnO₂ to begin accumulating by electrodeposition from the concentrated MnSO₄ electrolyte, and ϵ -MnO₂ is subsequently converted to Zn_xMn₂O₄. Electrodeposition of ϵ -MnO₂ lowers the electrolyte pH, dissolving ZHS from the surfaces of the cathode by cycle 10. During Stage II (Fig. 4), the electrolyte becomes depleted of Mn²⁺ and less ϵ -MnO₂ is formed with each subsequent cycle. Instead, tetragonal ZnMn₂O₄ is converted to a cubic phase by additional Zn²⁺ intercalation. The capacity for this process is low because the structure cannot accommodate much additional Zn²⁺. To attain high capacity operation, Zn²⁺ intercalation must be operated reversibly or avoided in order to leverage the full capability of the MnO₂ dissolution/redeposition mechanism (Fig. 1). The complexity of this process underscores the importance of choosing the proper current collector to study cathode AZIB electrochemistry to minimize side reactions and uncover the true mechanisms behind the observed capacity (Fig. 2).

In summary, the dynamics of the electrochemical interface at an AZIB cathode play a critical role in its performance and durability. The dissolution of MnO₂ was revealed, even in the presence of a highly concentrated Mn²⁺ electrolyte, and employed as a mechanism for a functioning battery. This insight was only possible after isolating the electrochemical reactions at the MnO₂ surface by eliminating any MnO₂ deposition on other conductive surfaces in the electrochemical cell. With this clear focus on the MnO₂ dissolution/redeposition dynamics, it is evident that developing the ability to facilitate the electrochemical instability of MnO₂ will be critical to the performance of Zn/MnO₂ batteries. Finally, this work provides guidance for expanding the concept and developing other systems that can reversibly deposit and dissolve the active material in a dynamic manner.

Methods

Chemicals

Manganese sulfate monohydrate (MnSO₄·H₂O, ACS reagent, ≥98%), potassium permanganate (KMnO₄, ACS reagent, ≥99.0%), and zinc sulfate heptahydrate (ZnSO₄·7H₂O, ≥99.0%) were purchased from

MilliporeSigma. Multi-walled carbon nanotubes (CNTs, ~140 nm diameter, ~7 μm length) were purchased from Strem Chemicals and multi-walled CNTs (~5-30 nm diameter, ~100 μm length) were purchased from NanoTechLabs, Inc. Isopropanol (IPA, ACS reagent, $\geq 99.5\%$) was purchased from VWR. Zn foil (0.25 mm thick, 99.98%) was purchased from Alfa Aesar. Hydrochloric acid (HCl, OmniTrace Ultra) and nitric acid (HNO_3 , OmniTrace Ultra) were purchased from Millipore Sigma.

Synthesis and Electrode Preparation

The synthesis of $\delta\text{-MnO}_2$ followed the procedure outlined in previous work¹⁸. Once dry, the powder was weighed for fabricating an electrode. The electrode was fabricated by a three-step filtration method⁵¹ that requires the preparation of three suspensions.

Suspension 1	~4 mg 7 μm CNTs	150 mL IPA
Suspension 2	~2 mg 7 μm CNTs + ~20.5 mg $\delta\text{-MnO}_2$	150 mL IPA
Suspension 3	~2 mg 7 μm CNTs + ~2 mg 100 μm CNTs	150 mL IPA

The suspensions were prepared by sonication until all materials were evenly dispersed. The vacuum filtration was performed by immediately filtering the suspensions in the order written above onto a 47 mm glass fiber filter (Pall Type A/E). The exposed area of the membrane is ~10.18 cm^2 , creating a loading of ~2.0 mg $\delta\text{-MnO}_2$ cm^{-2} , while the electrode content was ~67 wt% $\delta\text{-MnO}_2$.

Electrodes were punched to be 5/16" diameter and were individually weighed to determine the precise initial active mass by subtracting the mass of a 5/16" diameter glass fiber disk (3.58 ± 0.03 mg).

Electrochemistry

2032 coin cells were assembled in air atmosphere using either titanium (Ti, Grade 2, 0.005 in thick) or stainless steel (SS, Type 304, 0.5 mm thick) as current collector/spacer on the positive side. For all coin cells, two SS spacers were used, but both were placed on negative side if Ti was used on positive side. In coin cells without a $\delta\text{-MnO}_2$ electrode, a 16 mm glass fiber separator was placed over the positive electrode and soaked with 10 or 50 μL electrolyte, followed by 1/2" diameter Zn disk. Either 0.5 M ZnSO_4 or 0.5 M $\text{ZnSO}_4/0.5$ M MnSO_4 was used as electrolyte. When using a $\delta\text{-MnO}_2$ electrode, a 16 mm glass fiber separator with 1/4" hole in the center was placed over the electrode to maintain uniform thickness in the cell.

Coin cells were galvanostatically cycled at 0.1 mA (~100 mA/g initial active mass) between 0.9-1.9 V using a Maccor 4200 battery test system at room temperature. CV was performed at 0.5 mV s^{-1} between

0.9-1.9 V using an Autolab PGSTAT302N potentiostat.

***Ex situ* Precipitation of Zinc Hydroxide Sulfate**

10 mL of 0.5 M ZnSO₄/0.5 M MnSO₄ was placed in a glass vial with a stir bar. A certain volume of 0.1 M KOH was pipetted into the electrolyte while stirring, followed by inserting the pH electrode and measuring the pH with a Mettler Toledo SevenExcellence pH meter calibrated with three buffer solutions (pH = 4.01, 7.00, and 10.01). The volume of 0.1 M KOH added was increased from 20 to 40 to 80 to 200 μ L. After a total of 2.0 mL of 0.1 M KOH was added, the precipitate was centrifuged and dried at room temperature.

Materials Characterization

Coin cells were opened with a coin cell disassembling tool and the cathode was soaked in deionized water for 1 hour, followed by three additional rinses and drying in air at room temperature. Powder XRD was acquired using a Panalytical X'Pert Pro, Rigaku Miniflex, or Bruker D2 Phaser X-ray diffractometer (Cu K α radiation). Samples were placed on a zero-background silicon sample holder. PDF files used for reference were δ -MnO₂ (01-080-1098), ϵ -MnO₂ (00-030-0820), ZnMn₂O₄ (00-024-1133), Zn_{1.67}Mn_{1.33}O₄ (00-061-0716), ZHS·3H₂O (00-067-0055), ZHS·4H₂O (00-044-0673), and ZHS·5H₂O (00-060-0655).

Rietveld refinement was performed using TOPAS 5⁵². TEM images were acquired with a JEOL JEM-2100F FETEM at 200 kV accelerating voltage. ICP-MS data was acquired using a PerkinElmer NexION 350S. Samples were scraped from an electrode and digested in aqua regia prepared with a 3:1 volume ratio of HCl to HNO₃. Samples were then diluted to < 100 ppb Mn and Zn with deionized water. X-ray absorption near-edge structure (XANES) measurements were acquired at beamline 12-BM-B at the Advanced Photon Source at Argonne National Laboratory. XANES data was acquired at the Mn K-edge in transmission mode due to the uniformity of the electrodes prepared by filtration method. Spectra were simultaneously acquired on Mn foil in transmission mode for energy calibration. XANES data were calibrated and normalized in Athena, which was also used for linear combination fitting (LCF)⁵³. LCF was performed using the Combo method, which uses 17 pure valence Mn standards available from the original reference⁵⁴. During LCF, the sum of the components was constrained to one, but the contribution from each component was allowed to float positively or negatively. The most negative component was removed during each round of LCF until a fit with only positive contributions was obtained.

Declarations

Data Availability

The data that support the findings of this study are available from the corresponding author upon reasonable request.

Acknowledgements

Work by P.P.L., N.M.M., and S.T. was supported as part of the Joint Center for Energy Storage Research (JCESR), an Energy Innovation Hub funded by the U.S. Department of Energy, Office of Science, Basic Energy Sciences. Work by N.B. was supported by Laboratory Directed Research and Development (LDRD) funding from Argonne National Laboratory, provided by the Director, Office of Science, of the U.S. Department of Energy under Contract No. DE-AC02-06CH11357. Work by V.R.S., T.H., X.Z, D.Y.C., and M.G.K was supported by the U.S. Department of Energy, Office of Science, Office of Basic Energy Sciences, Materials Sciences and Engineering Division. Use of the Center for Nanoscale Materials, an Office of Science user facility, was supported by the U.S. Department of Energy, Office of Science, Office of Basic Energy Sciences, under Contract No. DE-AC02-06CH11357. This research used resources of the Advanced Photon Source, a U.S. Department of Energy (DOE) Office of Science User Facility operated for the DOE Office of Science by Argonne National Laboratory under Contract No. DE-AC02-06CH11357. We thank S. Lee for help in setting up XANES measurements at APS beamline 12-BM-B. We thank J. F. Mitchell for access to the Panalytical X'Pert Pro.

Author Contributions

N.B., S.T., and V.R.S. conceived the idea and designed the experiments. N.B. performed synthesis, electrochemistry, XANES analysis, and some XRD measurements. P.P.L. and N.B. conducted ICP-MS analysis. T.H. and N.B. conducted XANES measurements. X.Z., D.Y.C., and M.G.K. executed some XRD measurements and Rietveld refinement. B.F. executed some XRD measurements. Y.L. carried out HRTEM imaging. N.B., P.P.L., T.H., N.M.M., S.T., and V.R.S. discussed the results. N.B., S.T., P.P.L., T.H., and V.R.S. drafted the manuscript. All authors approved the final version of the manuscript.

Competing Interests

The authors declare no competing interests.

References

1. Ziegler, M. S. *et al.* Storage requirements and costs of shaping renewable energy toward grid decarbonization. *Joule* **3**, 2134–2153 (2019).
2. Argyrou, M. C., Christodoulides, P. & Kalogirou, S. A. Energy storage for electricity generation and related processes: Technologies appraisal and grid scale applications. *Renew. Sust. Energ. Rev.* **94**, 804–821 (2018).
3. Gür, T. M. Review of electrical energy storage technologies, materials and systems: challenges and prospects for large-scale grid storage. *Energ. Environ. Sci.* **11**, 2696–2767 (2018).
4. Lopes, P. P. & Stamenkovic, V. R. Past, present, and future of lead–acid batteries. *Science* **369**, 923–924 (2020).
5. Jia, X., Liu, C., Neale, Z. G., Yang, J. & Cao, G. Active materials for aqueous zinc ion batteries: synthesis, crystal structure, morphology, and electrochemistry. *Chem. Rev.* **120**, 7795–7866 (2020).
6. Wei, S. *et al.* A stable room-temperature sodium–sulfur battery. *Nat. Commun.* **7**, 11722, (2016).

7. Deng, Y.-P. *et al.* The current state of aqueous Zn-based rechargeable batteries. *ACS Energ. Lett.* **5**, 1665–1675 (2020).
8. Fang, G., Zhou, J., Pan, A. & Liang, S. Recent advances in aqueous zinc-ion batteries. *ACS Energ. Lett.* **3**, 2480–2501 (2018).
9. Blanc, L. E., Kundu, D. & Nazar, L. F. Scientific challenges for the implementation of Zn-ion batteries. *Joule* **4**, 771–799 (2020).
10. Konarov, A. *et al.* Present and future perspective on electrode materials for rechargeable zinc-ion batteries. *ACS Energ. Lett.* **3**, 2620–2640 (2018).
11. Mathew, V. *et al.* Manganese and vanadium oxide cathodes for aqueous rechargeable zinc-ion batteries: A focused view on performance, mechanism, and developments. *ACS Energ. Lett.* **5**, 2376–2400 (2020).
12. Senguttuvan, P. *et al.* A high power rechargeable nonaqueous multivalent Zn/V2O5 battery. *Adv. Energy Mater.* **6**, 1600826 (2016).
13. Kundu, D., Adams, B. D., Duffort, V., Vajargah, S. H. & Nazar, L. F. A high-capacity and long-life aqueous rechargeable zinc battery using a metal oxide intercalation cathode. *Nat. Energy* **1**, 16119 (2016).
14. Zhang, L., Chen, L., Zhou, X. & Liu, Z. Towards high-voltage aqueous metal-ion batteries beyond 1.5 V: the zinc/zinc hexacyanoferrate system. *Adv. Energy Mater.* **5**, 1400930 (2015).
15. Trócoli, R. & La Mantia, F. An aqueous zinc-ion battery based on copper hexacyanoferrate. *ChemSusChem* **8**, 481–485 (2015).
16. Shoji, T., Hishinuma, M. & Yamamoto, T. Zinc-manganese dioxide galvanic cell using zinc sulphate as electrolyte. Rechargeability of the cell. *J. Appl. Electrochem.* **18**, 521–526 (1988).
17. Xu, C., Du, H., Li, B., Kang, F. & Zeng, Y. Reversible insertion properties of zinc ion into manganese dioxide and its application for energy storage. *Electrochem. Solid St.* **12**, A61-A65 (2009).
18. Han, S.-D. *et al.* Mechanism of Zn insertion into nanostructured δ -MnO₂: A nonaqueous rechargeable Zn metal battery. *Chem. Mater.* **29**, 4874–4884, (2017).
19. Zhang, K. *et al.* Nanostructured Mn-based oxides for electrochemical energy storage and conversion. *Chem. Soc. Rev.* **44**, 699–728 (2015).
20. Zhan, C., Wu, T., Lu, J. & Amine, K. Dissolution, migration, and deposition of transition metal ions in Li-ion batteries exemplified by Mn-based cathodes—a critical review. *Energ. Environ. Sci.* **11**, 243–257 (2018).
21. Wang, X. *et al.* Boosting zinc-ion storage capability by effectively suppressing vanadium dissolution based on robust layered barium vanadate. *Nano Lett.* **20**, 2899–2906 (2020).
22. Lu, J. *et al.* Effectively suppressing dissolution of manganese from spinel lithium manganate via a nanoscale surface-doping approach. *Nat. Commun.* **5**, 5693 (2014).
23. Liu, T. *et al.* Correlation between manganese dissolution and dynamic phase stability in spinel-based lithium-ion battery. *Nat. Commun.* **10**, 4721 (2019).

24. Xu, G., Liu, Z., Zhang, C., Cui, G. & Chen, L. Strategies for improving the cyclability and thermostability of LiMn₂O₄-based batteries at elevated temperatures. *J. Mater. Chem. A* **3**, 4092–4123 (2015).
25. Xu, G.-L. *et al.* Building ultraconformal protective layers on both secondary and primary particles of layered lithium transition metal oxide cathodes. *Nat. Energy* **4**, 484–494 (2019).
26. Kim, S. H. & Oh, S. M. Degradation mechanism of layered MnO₂ cathodes in Zn/ZnSO₄/MnO₂ rechargeable cells. *J. Power Sources* **72**, 150–158 (1998).
27. Alfaruqi, M. H. *et al.* Structural transformation and electrochemical study of layered MnO₂ in rechargeable aqueous zinc-ion battery. *Electrochim. Acta* **276**, 1–11 (2018).
28. Chamoun, M., Brant, W. R., Tai, C.-W., Karlsson, G. & Noréus, D. Rechargeability of aqueous sulfate Zn/MnO₂ batteries enhanced by accessible Mn²⁺ ions. *Energ. Stor. Mater.* **15**, 351–360 (2018).
29. Pan, H. *et al.* Reversible aqueous zinc/manganese oxide energy storage from conversion reactions. *Nat. Energy* **1**, 16039 (2016).
30. Zhang, N. *et al.* Rechargeable aqueous zinc-manganese dioxide batteries with high energy and power densities. *Nat. Commun.* **8**, 405 (2017).
31. Chao, D. *et al.* An electrolytic Zn–MnO₂ battery for high-voltage and scalable energy storage. *Angew. Chem. Int. Edit.* **58**, 7823–7828 (2019).
32. Li, Y. *et al.* Reaction mechanisms for long-life rechargeable Zn/MnO₂ batteries. *Chem. Mater.* **31**, 2036–2047 (2019).
33. Xu, D. *et al.* Preparation and characterization of MnO₂/acid-treated CNT nanocomposites for energy storage with zinc ions. *Electrochim. Acta* **133**, 254–261 (2014).
34. Zhu, C. *et al.* Binder-free stainless steel@ Mn₃O₄ nanoflower composite: a high-activity aqueous zinc-ion battery cathode with high-capacity and long-cycle-life. *J. Mater. Chem. A* **6**, 9677–9683 (2018).
35. Qiu, C. *et al.* The function of Mn²⁺ additive in aqueous electrolyte for Zn/ δ -MnO₂ battery. *Electrochim. Acta* **351**, 136445 (2020).
36. Huang, Y. *et al.* Novel insights into energy storage mechanism of aqueous rechargeable Zn/MnO₂ batteries with participation of Mn²⁺. *Nano-Micro Lett.* **11**, 49 (2019).
37. Soundharajan, V. *et al.* The dominant role of Mn²⁺ additive on the electrochemical reaction in ZnMn₂O₄ cathode for aqueous zinc-ion batteries. *Energ. Stor. Mater.* **28**, 407–417 (2020).
38. Li, M. *et al.* A novel dendrite-free Mn²⁺/Zn²⁺ hybrid battery with 2.3 V voltage window and 11000-cycle lifespan. *Adv. Energy Mater.* **9**, 1901469 (2019).
39. Chao, D. *et al.* Atomic engineering catalyzed MnO₂ electrolysis kinetics for a hybrid aqueous battery with high power and energy density. *Adv. Mater.* **32**, 2001894 (2020).
40. Kang, C., Fang, J., Fu, L., Li, S. & Liu, Q. Hierarchical carbon nanowires/Ni@MnO₂ nanocomposites for high-performance asymmetric supercapacitors. *Chem.–Eur. J.* (2020).

41. Liu, C. *et al.* Tuning Mn²⁺ additive in the aqueous electrolyte for enhanced cycling stability of birnessite electrodes. *Electrochim. Acta* **298**, 678–684 (2019).
42. Bischoff, C. F. *et al.* Revealing the local pH value changes of acidic aqueous zinc ion batteries with a manganese dioxide electrode during cycling. *J. Electrochem. Soc.* **167**, 020545 (2020).
43. Lee, B. *et al.* Critical role of pH evolution of electrolyte in the reaction mechanism for rechargeable zinc batteries. *ChemSusChem* **9**, 2948–2956 (2016).
44. Shoji, T. & Yamamoto, T. Charging and discharging behavior of zinc–manganese dioxide galvanic cells using zinc sulfate as electrolyte. *J. Electroanal. Chem.* **362**, 153–157 (1993).
45. Moezzi, A., Cortie, M. B. & McDonagh, A. M. Zinc hydroxide sulphate and its transformation to crystalline zinc oxide. *Dalton T.* **42**, 14432–14437 (2013).
46. Peiteado, M., Sturm, S., Caballero, A. & Makovec, D. Mn₃ – xZn_xO₄ spinel phases in the Zn–Mn–O system. *Acta Mater.* **56**, 4028–4035 (2008).
47. Lee, J.-W., Seo, S.-D. & Kim, D.-W. Comparative study on ternary spinel cathode Zn–Mn–O microspheres for aqueous rechargeable zinc-ion batteries. *J. Alloy. Compd.* **800**, 478–482 (2019).
48. Knight, J. C., Therese, S. & Manthiram, A. Chemical extraction of Zn from ZnMn₂O₄-based spinels. *J. Mater. Chem. A* **3**, 21077–21082 (2015).
49. Nolis, G. M. *et al.* Electrochemical reduction of a spinel-type manganese oxide cathode in aqueous electrolytes with Ca²⁺ or Zn²⁺. *J. Phys. Chem. C* **122**, 4182–4188 (2018).
50. Park, M. J., Yaghoobnejad Asl, H. & Manthiram, A. Multivalent-ion versus proton insertion into battery electrodes. *ACS Energ. Lett.* **5**, 2367–2375 (2020).
51. Lee, E. *et al.* Design of lithium cobalt oxide electrodes with high thermal conductivity and electrochemical performance using carbon nanotubes and diamond particles. *Carbon* **129**, 702–710 (2018).
52. Coelho, A. A. TOPAS and TOPAS-Academic: an optimization program integrating computer algebra and crystallographic objects written in C++. *J. Appl. Cryst.* **51**, 210–218 (2018).
53. Ravel, B. & Newville, M. ATHENA, ARTEMIS, HEPHAESTUS: data analysis for X-ray absorption spectroscopy using IFEFFIT. *J. Synchrotron Radiat.* **12**, 537–541 (2005).
54. Manceau, A., Marcus, M. A. & Grangeon, S. Determination of Mn valence states in mixed-valent manganates by XANES spectroscopy. *Am. Mineral.* **97**, 816–827 (2012).

Figures

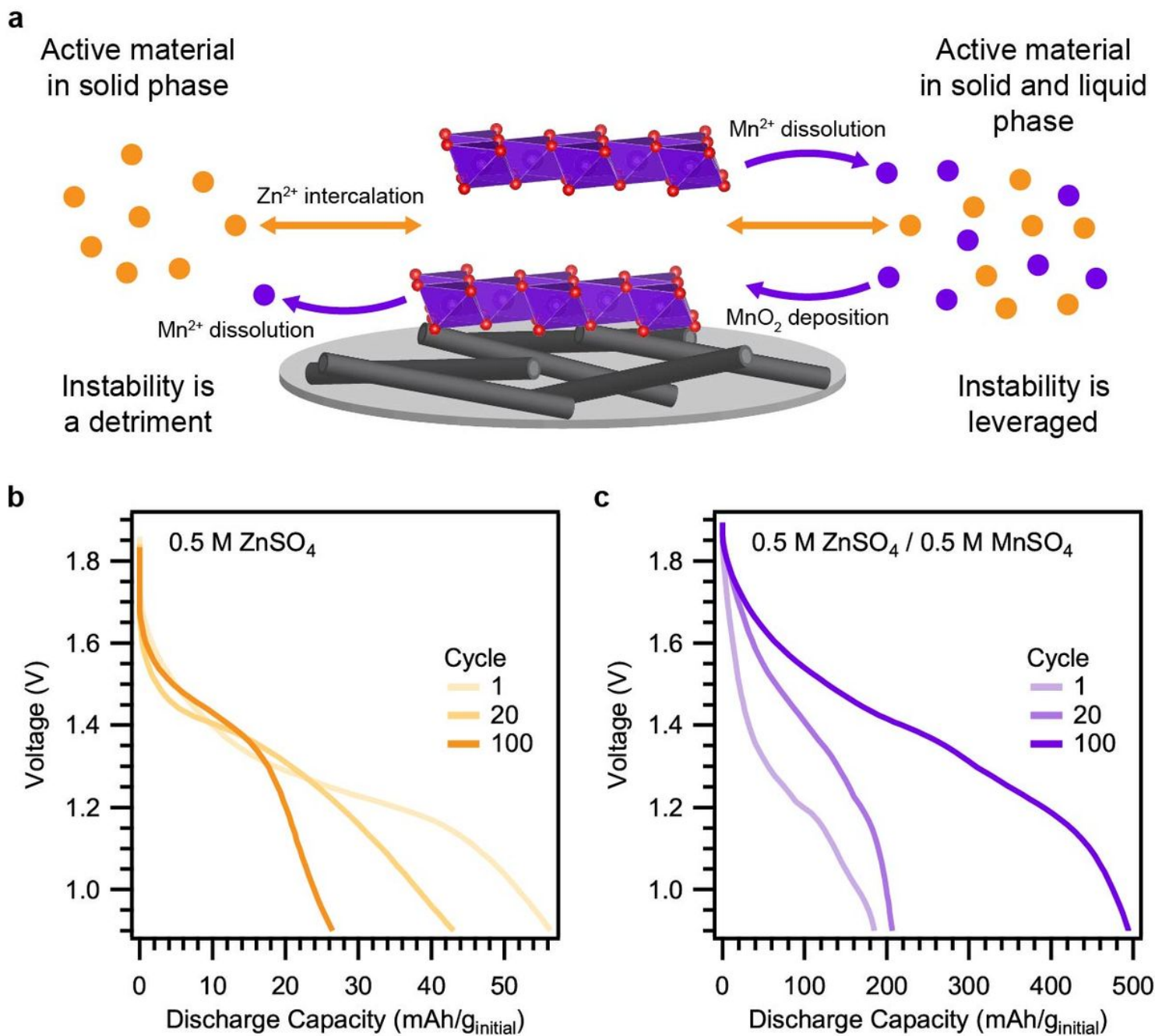


Figure 1

Mechanisms of operation for a MnO_2 cathode in an AZIB. a Scheme of possible processes occurring during AZIB cycling. Orange-Zn, purple-Mn, red-O. Discharge capacity of Zn/ MnO_2 AZIB with b $Zn^{2+}(aq)$ -only electrolyte or c $Zn^{2+}(aq)$ - $Mn^{2+}(aq)$ electrolyte.

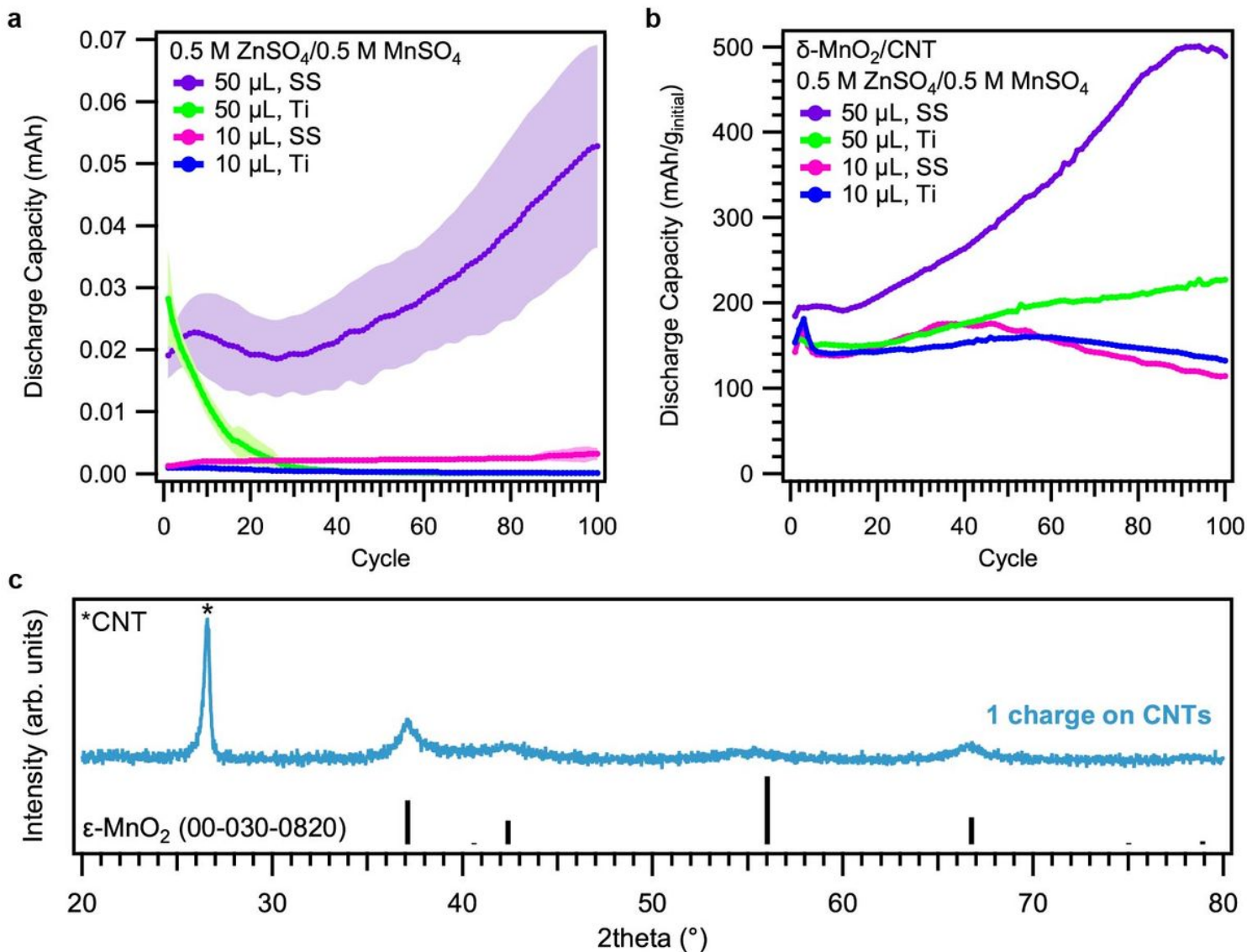


Figure 2

Effect of current collector on AZIB performance. a Discharge capacity of coin cells with either SS or Ti cathode and Zn anode in different volumes of Zn²⁺(aq)-Mn²⁺(aq) electrolyte (shaded area indicates standard deviation of three cells). b Discharge capacity of δ -MnO₂/CNT cathode with either SS or Ti supporting current collector. c XRD of CNT cathode after charging once in Zn²⁺(aq)-Mn²⁺(aq) electrolyte.

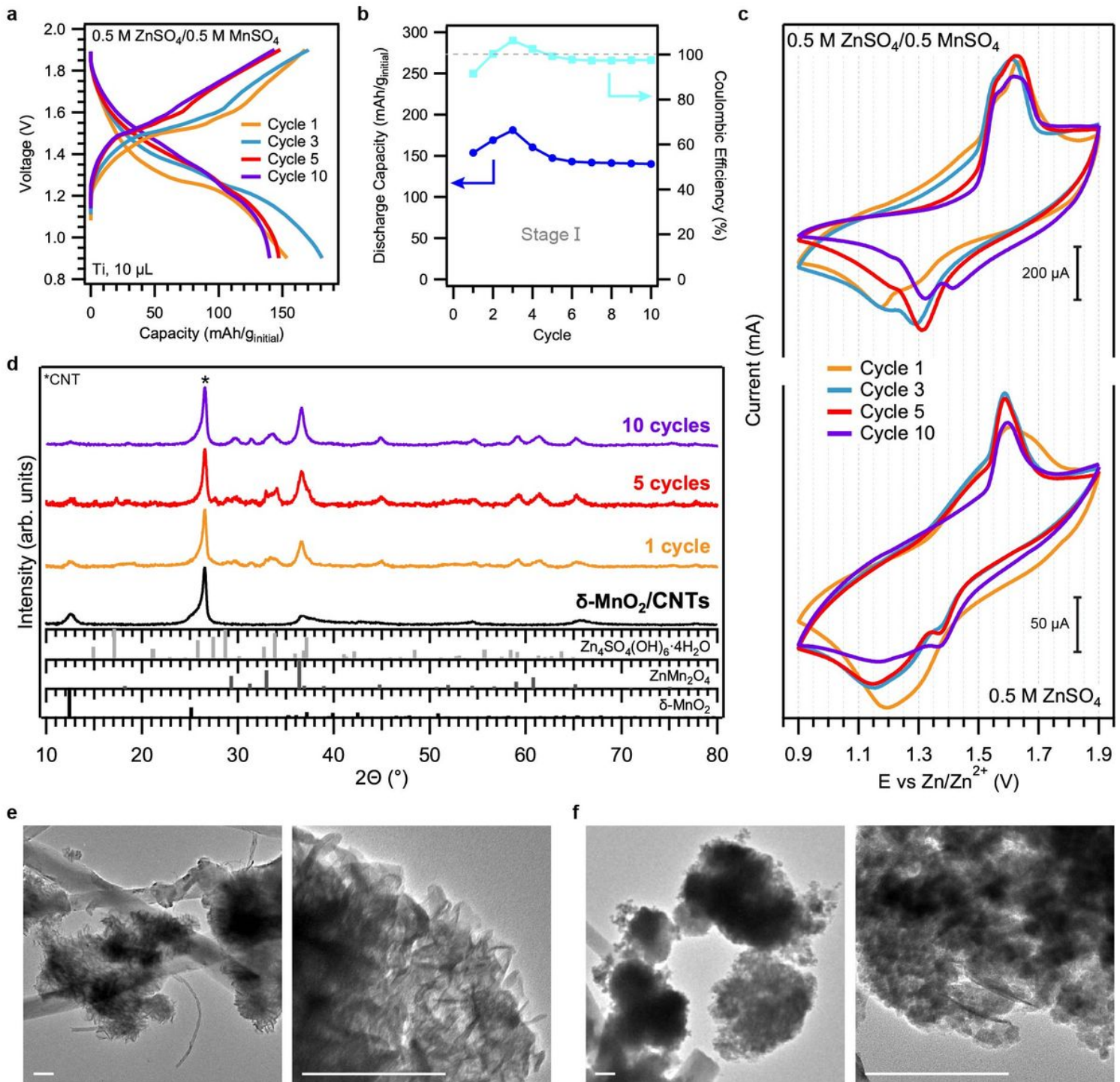


Figure 3

Impact of MnO₂ dissolution on transformation of AZIB cathode. a Selected cycles of AZIB with δ-MnO₂/CNT cathode on Ti current collector, Zn²⁺(aq)-Mn²⁺(aq) electrolyte, and Zn anode. b Discharge capacity, normalized to initial mass of δ-MnO₂, and CE over first 10 cycles. c CV of AZIB in Zn²⁺(aq)-Mn²⁺(aq) and Zn²⁺(aq)-only electrolytes. d XRD of cathode in discharged state after 1, 5, or 10 cycles. TEM images (scale bars = 200 nm) of e the as-prepared δ-MnO₂/CNT electrode and f the electrode after 5th discharge in Zn²⁺(aq)-Mn²⁺(aq) electrolyte.

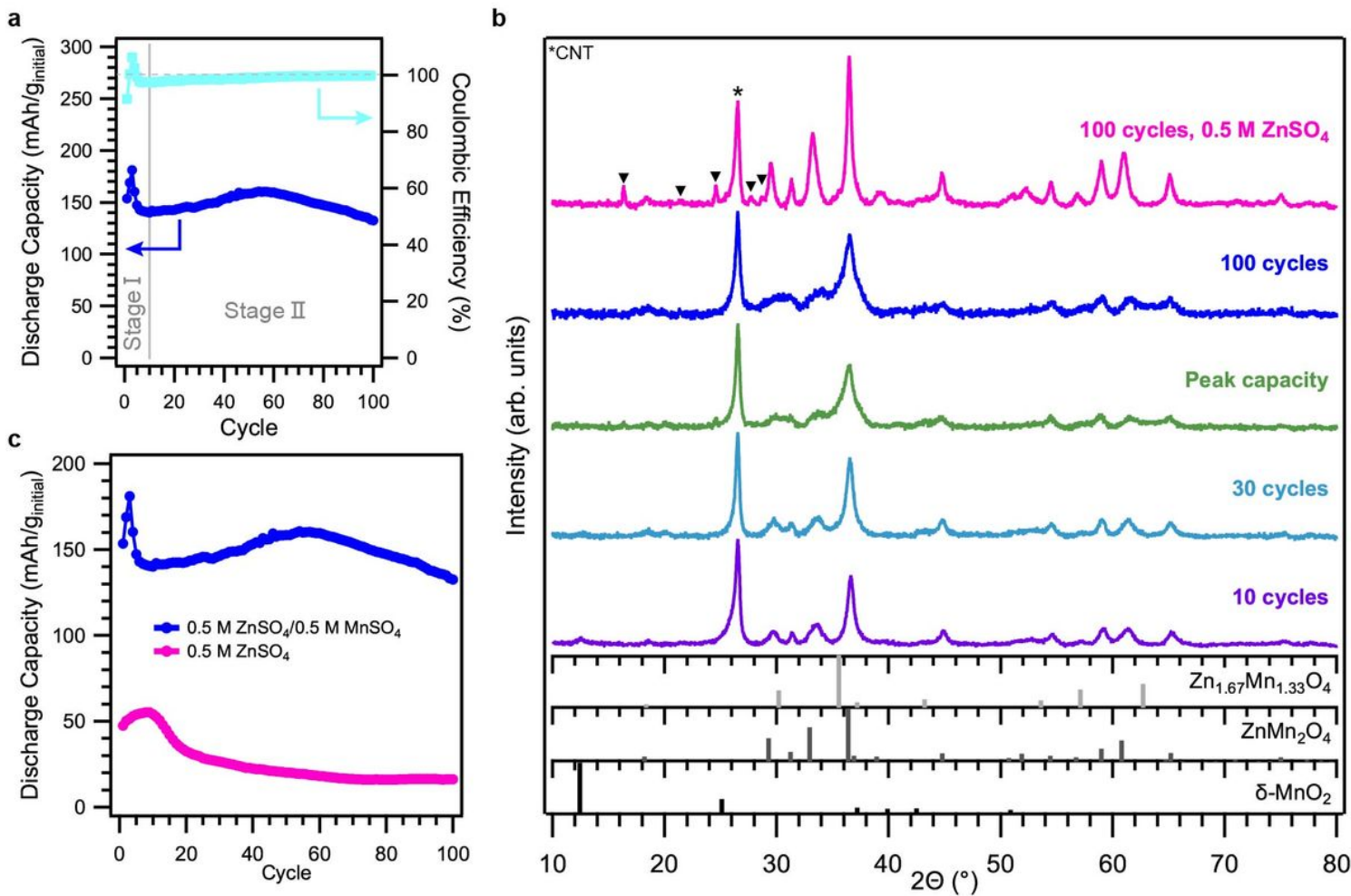
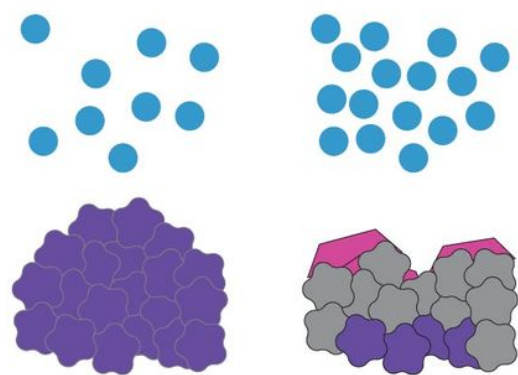


Figure 4

MnO₂ dissolution/redeposition during long-term AZIB cycling. a Discharge capacity (normalized to initial mass of δ-MnO₂) and CE for AZIB with δ-MnO₂/CNT cathode, Zn²⁺(aq)-Mn²⁺(aq) electrolyte, and Zn anode. b XRD of AZIB cathode in discharged state after various numbers of cycles in Zn²⁺(aq)-Mn²⁺(aq) electrolyte and after 100 cycles in Zn²⁺(aq)-only electrolyte (▼ indicates ZHS). c Performance of AZIB with or without MnSO₄ in electrolyte.

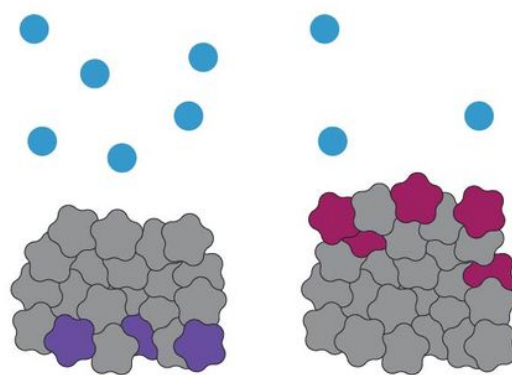
Stage I



Cycle 0

Cycle 5

Stage II



Cycle 10

Cycle 100

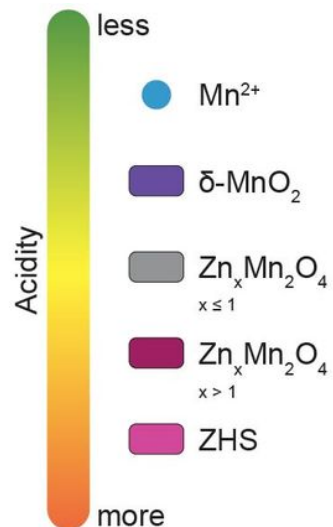


Figure 5

Transformation of the electrochemical interface at a dynamic δ -MnO₂ cathode. The qualitative cathode composition and electrolyte Mn²⁺ concentration and pH are depicted at selected cycles in the discharged state over the lifetime of the AZIB.

Supplementary Files

This is a list of supplementary files associated with this preprint. Click to download.

- [EmployingthedynamicsSI.docx](#)